Emergence of paraelectric, improper antiferroelectric, and proper ferroelectric nematic phases in a liquid crystal composed of polar molecules

A. V. Emelyanenko,[1,*] V. Yu. Rudyak,[1] S. A. Shvetsov,[1,2] F. Araoka,[3] H. Nishikawa,[3] and K. Ishikawa[4]

[1]*Lomonosov Moscow State University, Moscow 119991, Russia*

[2]*Lebedev Physical Institute, Moscow 119991, Russia*

[3]*RIKEN Center for Emergent Matter Science (CEMS), 2-1 Hirosawa Wako, Saitama 351-0198, Japan*

[4]*Tokyo Institute of Technology, 2-12-1 Ookayama, Meguro-ku, Tokyo 152-8550, Japan*

(Received 5 February 2022; accepted 13 May 2022; published 3 June 2022)

We have elaborated a theoretical approach for the description of polar nematic phases observed by Nishikawa *et al.* [Adv. Mater. **29**, 1702354 (2017)], their structures, and transitions between them. Specific symmetry contributions to the pair molecular potentials provide the molecular mechanisms responsible for the formation of proper and improper polarity on the macroscopic level. An improper antiferroelectric nematic M2 phase can arise between paraelectric nematic M1 and proper ferroelectric nematic MP in the temperature scale. The local polarization in M2 arises mostly due to the local splay deformation. The director distribution in M2 represents the conjugation of cylindrical waves with opposite splay and polarization signs. The director and polarization are parallel to the cylindrical domain axes in the middle of each cylinder but exhibit considerable (mostly radial) deformation on the periphery of each cylinder. Polarization vectors are mostly stacked antiparallel on the borders between the domains without the director disruption. The domain size decreases with the decreasing temperature, the percentage of the antiferroelectric decouplings increases, and M2 exhibits the first-order phase transition into proper ferroelectric MP. With the increasing temperature the domain size in the M2 phase increases, the domination of particular polar orientation of molecules reduces, and finally, the domain size diverges at particular temperature corresponding to the second-order phase transition from M2 to paraelectric M1. Variations of the polar and nonpolar orientational order parameters are estimated within each phase and between the phases. Our experimental and computer simulation results (also presented in the paper) fully support our theoretical findings.

DOI: 10.1103/PhysRevE.105.064701

I. INTRODUCTION

Liquid crystals are important materials for many applications, such as modern display technologies [1–4], light modulators and filters [5,6], chemical and other sensors [7–11], microwave, and millimeter wave electronics (phase shifters, filters, antennas, etc.) [12,13]. Recently, a new class of liquid crystalline materials was developed, the so-called "polar nematics" [14–18]. They have extraordinary large polarization and, at the same time, possess nematic ordering. Polar nematics have great potential in many research fields, such as electronics and electro-optics [14,19], nonlinear optics [16], and many others.

Symmetry arguments for the existence of ferroelectricity in liquid crystals were considered and confirmed by Meyer [20,21]. Antiferroelectric and several intermediate (ferrielectric) phases were discovered by Fukuda and co-workers in Refs. [22–24]. Most of the phases reported in these and other papers are *improper* ferroelectric or antiferroelectric [25], because polarization in these phases is not the phase transition parameter. Meanwhile, several publications [26–29] reported on the so-called "re-entrant" ferroelectric phase. The origin of this phase was investigated later in Ref. [30], and this phase was found to be the *proper* ferroelectric, because the interactions of dipoles located in the long molecular tails solely induce the polarization (no other polar vectors and parameters are needed for characterization of the phase) and trigger the reentrance of ferroelectricity. Up to recent times, this was the only ferroelectric phase in low-mass liquid crystal melts, whose origin was addressed to the proper ferroelectricity.

In 2017 the existence of a polar nematic (MP) phase was reported in the DIO liquid crystal [14]. It was registered on the cooling cycle from the paraelectric nematic M1 phase, while some nontrivial intermediate phase (designated as M2) was registered between the M1 and MP phases in the temperature scale. The M2 phase appeared to be spontaneously deformed (with the nonuniform director distribution). The transition between the MP and M2 phases is of the first order, while the transition between the M1 and M2 phases was reported to be of the second order in Ref. [15]. It should be also mentioned that the direct second-order phase transition between the MP and M1 phases was also observed in different material in Ref. [15]. The existence of the M2 phase should be addressed to the fact that the molecules of DIO are polar and should better fit each other in the space if they are organized in some locally splayed domains. In this case, the role of flexoelectric polarization is important. The lattice model for the splay flexoelectric effect in nematic liquid crystals was considered by Dhakal and Selinger [31], and the transitions between isotropic, nematic, and polar phases were

*emel@polly.phys.msu.ru

described using Monte Carlo simulations. Recently, a novel splay nematic phase was reported by Mertelj and co-workers [32]. The phase transition between the splay nematic phase and conventional nematic phase was reported in Ref. [33] to be a weak first-order phase transition and described in the framework of phenomenological Landau–de Gennes theory in Ref. [34]. The single and double splay waves were predicted in Refs. [35,36] as possible structures of the splay nematic phase. An important role of the flexoelectric effect in the formation of the splay nematic phase has been outlined. The mechanism responsible for elastic constant softening was reported in Ref. [37]. Here we expect that the M2 phase observed in DIO material is the splay nematic phase and provide a theoretical approach describing the structures and transitions between the M1, M2, and MP phases, based on molecular symmetry arguments and statistical distributions. We also derive a simple analytical equation describing the structure of the double splay phase following from minimization of the free energy.

The paper is organized as follows. In Sec. II the experimental results for DIO material are presented. In Sec. III the molecular model is considered and the specific polar-symmetry intermolecular interaction terms found. In Sec. IV the director distribution in a nematic phase composed of polar molecules is obtained by minimization of the elastic energy following from intermolecular interaction. In Sec. V the results of computer simulations for the director distribution in polar nematic material are presented. In Sec. VI the space distributions and temperature dependencies of the polar and nonpolar orientational order parameters are found, and the transitions between M1, M2, and MP phases are described. Finally, in Sec. VII the conclusions are made.

II. OPTICAL ANISOTROPY OF DIO COMPOUND

Let us start with consideration of optical properties of the DIO compound. Ferroelectric ordering in the MP phase was confirmed previously in Ref. [14], while the existence of antiferroelectric domains in the M2 phase was confirmed in Ref. [15]. Therefore, in our experiment we have concentrated on the observation of microscopic images of all the phases and birefringence measurements. The temperature dependence of optical anisotropy $\Delta n(T)$, i.e., the difference between the extraordinary and ordinary refractive indices, is the important characteristic of any liquid crystal (LC) material. The initial measurement was performed in Ref. [15], but it requires some clarification in the vicinity of phase transitions.

For this purpose we carried out the optical retardance measurement for a planar LC cell of thickness of 5.0 μm using a Berek compensator. Optical textures in crossed polarizers were observed with the help of a polarizing optical microscope (Nikon LV100N Pol, Japan) equipped with a heating stage (TMS-93 Stage Temp Controller and THMS 600 microscope stage, UK). The temperature variation rate was 0.1 °C/min in the vicinity of the phase transitions and 1 °C/min far from them. The optical retardance R was measured using a Berek compensator (Nichika, Japan). The optical anisotropy was determined as $\Delta n = R/\lambda$ ($\lambda = 550$ nm) with an accuracy of 0.005, first with the temperature decrease from isotropic phase and then with the temperature increase from polar phase (MP). This approach allows one to control the orientation and phase condition of the sample during the measurement.

First, the sample was heated to the isotropic state, and afterwards the temperature was gradually decreasing. At 175.6 °C, the stepwise isotropic-nematic (I-M1) phase transition happens and a clear planar alignment is formed [Fig. 1(a)]. Upon farther decrease of the temperature, the optical anisotropy Δn determined gradually increases from 0.07 to 0.18 (Fig. 2). Near $T = 69$ °C the texture distortion appears and a peculiarity of the $\Delta n(T)$ dependence is registered (see the insertion in Fig. 2), indicating perhaps some new phase, which is not discussed elsewhere and is also beyond the scope of the present paper. This distortion is better visible in the presence of the compensator plate, which indicates slight variations of director tilt or of the order parameter. About one degree below, the textures become uniform and the first-order phase transition (corresponding to the transition into the polar MP phase reported in [14]) happens. The color variation of the sample in crossed polarizers without compensator from yellow to red [Fig. 1(a), $T = 68.6$ °C] can originate from π-twisted structure formation in the MP phase [15]. The value of Δn varies stepwise from 0.19 to 0.23. The further temperature decrease slightly affects the optical anisotropy.

At the temperature increase from 42 °C, the $S(T)$ dependence repeats the one obtained on the cooling cycle. The difference is only in the appearance of slight texture distortion in the temperature range 69 °C $< T <$ 85 °C [Fig. 1(b)]. This temperature range corresponds to the range of existence of the intermediate M2 phase in the DIO material reported in [14] and arising between the polar MP and nonpolar M1 nematic phases. As in the aforementioned case, this distortion is clearly visible in the presence of the Berek compensator. At higher temperatures (85 °C $< T <$ 175.6 °C), the optical texture becomes uniform.

Since in Fig. 1 we observe the border between the M2 and MP phases, the stepwise growth of optical anisotropy at $T = 68.6$ °C should correspond to the phase transition. The symmetry change between the M2 and MP phases (MP is macroscopically polar while M2 is not, which is confirmed by the dielectric measurements in Ref. [14]) suggests that the M2-MP phase transition is of the first order, although the hysteresis is very weak. On the contrary, the M1-M2 phase transition does not cause a stepwise change in optical anisotropy.

III. MOLECULAR MODEL AND INTERMOLECULAR INTERACTION

Let us model a nematic phase composed of polar molecules (see Fig. 3).

In Ref. [14] it was discussed that the DIO liquid crystal composed of polar molecules can demonstrate several nematiclike phases. The higher-temperature M1 phase is paraelectric, the lower-temperature MP phase is ferroelectric, and the M2 phase observed between them in the temperature scale demonstrates some intermediate properties. All material properties usually arise on the molecular level. To outline the structures and properties of all these phases, let us consider

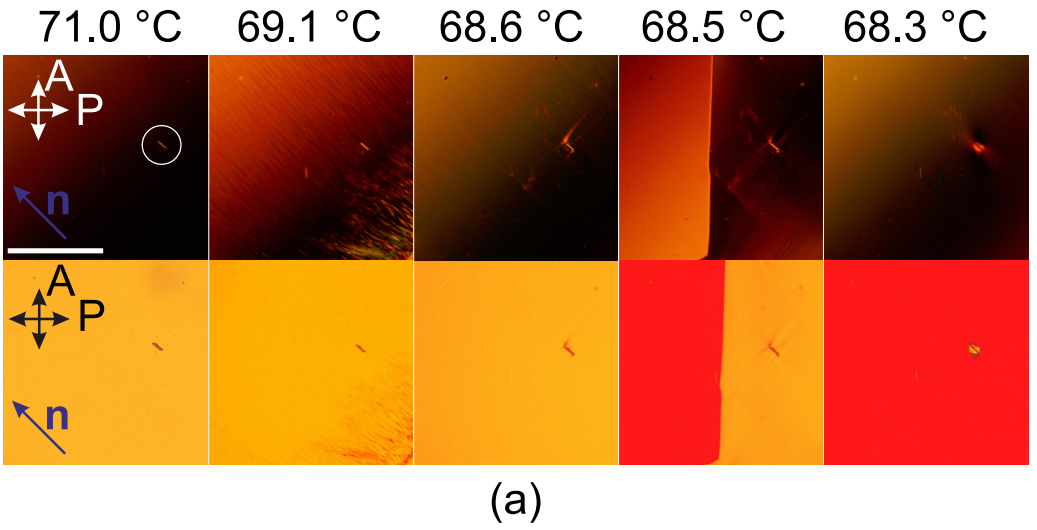

(a)

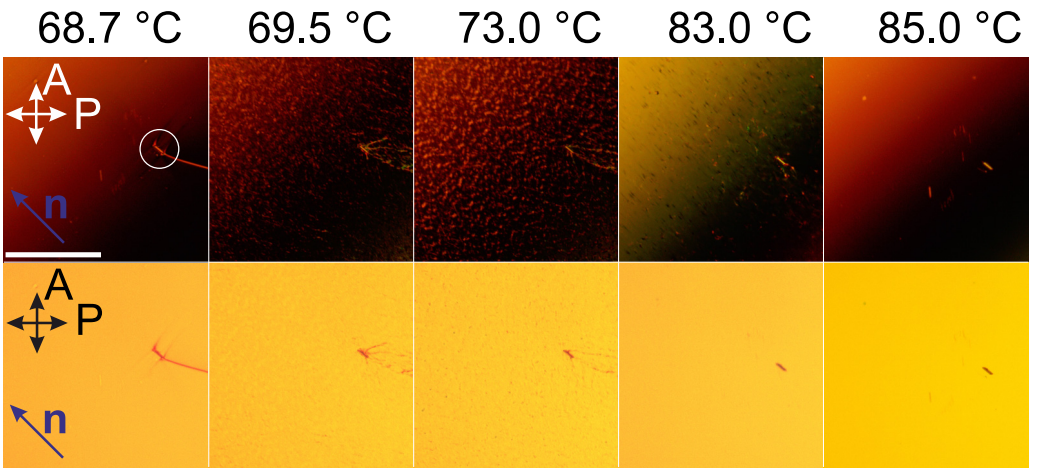

(b)

FIG. 1. Optical textures of the DIO film in 5-μm-thick planar cell during the temperature decrease (a) and increase (b). The upper lines in both (a) and (b) were obtained in the presence of a Berek compensator (the lower right corner of each picture corresponds to the complete phase shift compensation). Double arrows show the positions of polarizer (P) and analyzer (A). The arrow **n** shows the director alignment, and the white circle indicates the position of the spacer. The white scale bar is 200 μm.

various polar and nonpolar symmetries of the intermolecular potential.

For this purpose, let us consider a pair of molecules (Fig. 4) having principal molecular axes $\mathbf{a}_1$ and $\mathbf{a}_2$ and approximate the effective pair molecular interaction potential $U_{12}^{ef}(\mathbf{a}_1, \mathbf{a}_2, \mathbf{r}_{12})$ [where $\mathbf{r}_{12}$ is the intermolecular vector] by spherical invariants $T_{\ell L\lambda}(\mathbf{a}_1, \mathbf{u}_{12}, \mathbf{a}_2)$ [where $\mathbf{u}_{12} \equiv \mathbf{r}_{12}/|r_{12}|$ is the unit intermolecular vector] [38,39]:

$$U_{12}^{ef}(\mathbf{a}_1, \mathbf{a}_2, \mathbf{r}_{12}) = -\sum_{\ell,L,\lambda} J_{\ell L\lambda}(r_{12}) T_{\ell L\lambda}(\mathbf{a}_1, \mathbf{u}_{12}, \mathbf{a}_2). \quad (1)$$

Mathematically, they are the complete orthogonal set of functions of the three unit vectors: the principal axes of two interacting molecules $\mathbf{a}_1$ and $\mathbf{a}_2$, and the unit intermolecular vector $\mathbf{u}_{12}$. The useful property of spherical invariants is that their average with respect to each of the two molecular axes $\mathbf{a}_1$ and $\mathbf{a}_2$ is proportional to the orientational order parameter, which is the average Legendre polynomial of the same order as the corresponding index of spherical invariant reflecting the maximal power of the vector, over which it is averaged. Normally, only the nonpolar spherical invariants (with the even indexes) are considered:

$$\begin{aligned} T_{202}(\mathbf{a}_1, \mathbf{u}_{12}, \mathbf{a}_2) &= P_2(\mathbf{a}_1 \cdot \mathbf{a}_2) = \tfrac{3}{2}(\mathbf{a}_1 \cdot \mathbf{a}_2)^2 - \tfrac{1}{2}, \\ T_{220}(\mathbf{a}_1, \mathbf{u}_{12}, \mathbf{a}_2) &= P_2(\mathbf{a}_1 \cdot \mathbf{u}_{12}) = \tfrac{3}{2}(\mathbf{a}_1 \cdot \mathbf{u}_{12})^2 - \tfrac{1}{2}, \\ T_{022}(\mathbf{a}_1, \mathbf{u}_{12}, \mathbf{a}_2) &= P_2(\mathbf{a}_2 \cdot \mathbf{u}_{12}) = \tfrac{3}{2}(\mathbf{a}_2 \cdot \mathbf{u}_{12})^2 - \tfrac{1}{2}. \end{aligned} \quad (2)$$

Here we are going to take into account the polar spherical invariants (with the odd indexes) in addition:

$$\begin{aligned} T_{101}(\mathbf{a}_1, \mathbf{u}_{12}, \mathbf{a}_2) &= (\mathbf{a}_1 \cdot \mathbf{a}_2), \\ T_{110}(\mathbf{a}_1, \mathbf{u}_{12}, \mathbf{a}_2) &= (\mathbf{a}_1 \cdot \mathbf{u}_{12}), \\ T_{011}(\mathbf{a}_1, \mathbf{u}_{12}, \mathbf{a}_2) &= (\mathbf{a}_2 \cdot \mathbf{u}_{12}). \end{aligned} \quad (3)$$

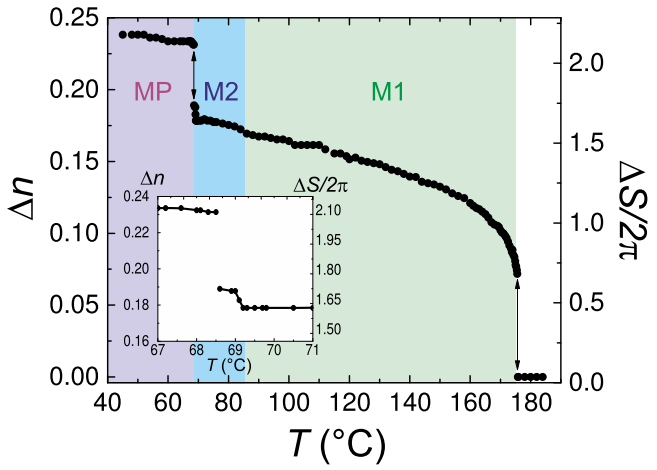

FIG. 2. The temperature dependence of the Δn optical anisotropy and ΔS phase shift between extraordinary and ordinary waves measured for DIO compound in 5-μm-thick planar cell.

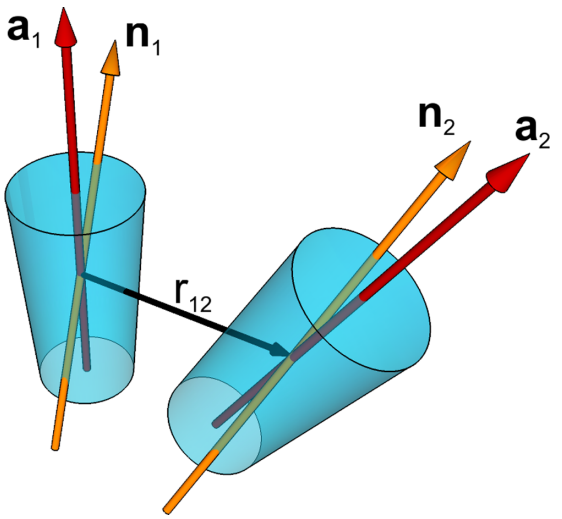

FIG. 4. Pair of interacting polar molecules in the inhomogeneous liquid crystal.

Invariant $T_{101}(\mathbf{a}_1, \mathbf{u}_{12}, \mathbf{a}_2)$ changes its sign if the axis of one molecule is reoriented in the opposite direction with respect to the axis of another molecule. In contrast, invariants $T_{110}(\mathbf{a}_1, \mathbf{u}_{12}, \mathbf{a}_2)$ and $T_{011}(\mathbf{a}_1, \mathbf{u}_{12}, \mathbf{a}_2)$ change their signs if the corresponding molecular axis ($\mathbf{a}_1$ or $\mathbf{a}_2$) is reoriented in the opposite direction with respect to the intermolecular vector $\mathbf{u}_{12}$. The average of invariants (2)–(3) with respect to the all three vectors $\mathbf{a}_1$, $\mathbf{a}_2$, and $\mathbf{u}_{12}$ contributes to the free energy. In Ref. [40] it was shown that the nonpolar spherical invariants contribute to the nonpolar molecular anisotropy and to the elastic constants. Here we are going to elucidate the role of the polar spherical invariants. In the deformed state, director $\mathbf{n}_2$ at point 2 where the second molecule is located is different from director $\mathbf{n}_1$ at point 1 where the first molecule is located (see Fig. 4), and therefore the gradient expansion of the director should be used:

$$\mathbf{n}_2 \approx \mathbf{n}_1 + (\mathbf{r}_{12}\cdot\nabla)\mathbf{n}_1 + \tfrac{1}{2}(\mathbf{r}_{12}\cdot\nabla)^2\mathbf{n}_1. \tag{4}$$

As a result, one obtains for the average $J_{101}(r_{12})\,T_{101}(\mathbf{a}_1, \mathbf{u}_{12}, \mathbf{a}_2)$ term with respect to all three vectors $\mathbf{a}_1$, $\mathbf{a}_2$, and $\mathbf{u}_{12}$,

$$\begin{aligned}&\langle J_{101}(r_{12})\,T_{101}(\mathbf{a}_1, \mathbf{u}_{12}, \mathbf{a}_2)\rangle \\ &\quad\approx J^{(0)}_{101}\,P^2 + \tfrac{1}{2}J^{(2)}_{101}\,P^2\,\langle \mathbf{n}\cdot(\mathbf{u}_{12}\cdot\nabla)^2\mathbf{n}\rangle,\end{aligned} \tag{5}$$

where the universal $\langle u_\alpha u_\beta\rangle = \frac{1}{3}\delta_{\alpha\beta}$ and $\langle u_\alpha\rangle = 0$ rules for the averages of projections of vector $\mathbf{u}_{12}$ on the Cartesian axes are

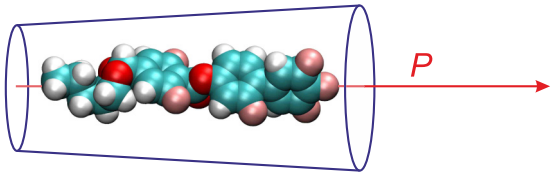

FIG. 3. Schematic representation of the DIO polar molecules [14].

used. The polar order parameter P is introduced in the same manner as the nonpolar order parameter S (both generally depend on coordinate $\mathbf{r}$),

$$\begin{aligned}P(\mathbf{r}) &\equiv \int f\{(\mathbf{a}\cdot\mathbf{n}), \mathbf{r}\}P_1(\mathbf{a}\cdot\mathbf{n})d^2\mathbf{a},\\ S(\mathbf{r}) &\equiv \int f\{(\mathbf{a}\cdot\mathbf{n}), \mathbf{r}\}P_2(\mathbf{a}\cdot\mathbf{n})d^2\mathbf{a},\end{aligned} \tag{6}$$

where $P_1(x) \equiv x$ and $P_2(x) \equiv 3/2\,x^2 - 1/2$ are the first and the second Legendre polynomials, $f\{(\mathbf{a}\cdot\mathbf{n}), \mathbf{r}\}$ is the orientational distribution function for molecules having principal axes $\mathbf{a}$ with respect to director $\mathbf{n}$ at point $\mathbf{r}$, and the $J^{(i)}_{\ell L\lambda}$ coefficients are generally introduced as follows:

$$J^{(i)}_{\ell L\lambda} \equiv \frac{1}{V_0}\int_0^\infty dr_{12} r_{12}^{i+2} J_{\ell L\lambda}(r_{12}), \tag{7}$$

where V_0 is the bulk occupied by a molecule and its nearest neighbors (see Ref. [40]). The polar order parameter P is different from zero if the orientational distribution function is nonsymmetrical (when the molecular long axes are distributed in a polar way). Electric polarization (its contribution along director) is equal to the multiple of the longitudinal molecular dipole and P. The first term in Eq. (5) contributes to the prime polar anisotropy, while, after substitution of gradient expansion (4), the average in the second term in Eq. (5) can be written as follows:

$$\begin{aligned}\langle \mathbf{n}\cdot(\mathbf{u}_{12}\cdot\nabla)^2\mathbf{n}\rangle = -\tfrac{1}{3}\{&(\nabla\cdot\mathbf{n})^2 + (\mathbf{n}\cdot[\nabla\times\mathbf{n})])^2\\ &+ [\mathbf{n}\times[\nabla\times\mathbf{n})]]^2 - \nabla\cdot(\mathbf{n}(\nabla\cdot\mathbf{n})\\ &- (\mathbf{n}\cdot\nabla)\mathbf{n})\},\end{aligned} \tag{8}$$

and thus does not bring us any new information, because it simply makes an additional contribution to the elastic energy in the one-constant approximation. In the same manner, let us average the $J_{110}(r_{12})\,T_{110}(\mathbf{a}_1, \mathbf{u}_{12}, \mathbf{a}_2)$ and $J_{011}(r_{12})\,T_{011}(\mathbf{a}_1, \mathbf{u}_{12}, \mathbf{a}_2)$ terms with respect to all three

vectors $\mathbf{a}_1$, $\mathbf{a}_2$, and $\mathbf{u}_{12}$:

$$\begin{aligned}&\langle J_{110}(r_{12})\, T_{110}(\mathbf{a}_1, \mathbf{u}_{12}, \mathbf{a}_2)\rangle \\ &= \langle J_{011}(r_{12})\, T_{011}(\mathbf{a}_1, \mathbf{u}_{12}, \mathbf{a}_2)\rangle \\ &\approx \tfrac{1}{2} P\left[J^{(1)}_{110} + J^{(1)}_{011}\right]\langle \mathbf{u}_{12}\cdot(\mathbf{u}_{12}\cdot\nabla)\mathbf{n}\rangle \\ &= \tfrac{1}{6} P\left[J^{(1)}_{110} + J^{(1)}_{011}\right](\nabla\cdot\mathbf{n}). \end{aligned} \tag{9}$$

Term (9) is the flexoelectric term having exactly the same form as in Refs. [31–37] but obtained from intermolecular interaction of particular symmetry. This term is exclusively important in our consideration, because it appears to be the splay generator in the molecular system composed of polar molecules. It also generates polarization (nonzero polar order parameter P), which appears to be *improper*, in contrast to polarization arising because of the $J^{(0)}_{101}$ term [the first term in the right-hand side of Eq. (5)], which is *proper*. Indeed, in the $T_{101}(\mathbf{a}_1, \mathbf{u}_{12}, \mathbf{a}_2)$ invariant, the polar axis of one molecule couples to the polar axis of another molecule; no coupling with other vectors is present; P^2 appears in average; a polar state without splay and bend deformations arises at P different from zero; and P is the only transition parameter in the absence of other terms. In contrast, in the $T_{110}(\mathbf{a}_1, \mathbf{u}_{12}, \mathbf{a}_2)$ and $T_{011}(\mathbf{a}_1, \mathbf{u}_{12}, \mathbf{a}_2)$ invariants, the polar axis couples to the intermolecular vector; P in the first power appears in average and couples to the splay; and the splay phase with local polarization arises when both P and splay are present and does not arise when either P or splay are absent. Below it is shown that the antiferroelectric domains should arise in the improper phase; no polarization appears in average over the domain in the absence of other terms, and thus, polarization is not the transition parameter; and the domain length is the transition parameter.

If the molecule has transverse dipole, polarization can also have nonzero contribution in the direction perpendicular to director. But in this case, the structure should be macroscopically biaxial [41]. Since the DIO molecules do not possess any pronounced biaxiality, the molecular short axes are expected to be distributed randomly. In this case, flexo-polarization can only appear as a result of the splay deformation. The statistical approach derived in Sec. VI will allow us to estimate the flexoelectric constant in the DIO material from the M2–M1 transition temperature measured experimentally in Refs. [14,15].

IV. DIRECTOR DISTRIBUTION IN A NEMATIC PHASE COMPOSED OF POLAR MOLECULES

We expect that the molecules of nematic liquid crystal can be locally organized in the nonpolar nondeformed, polar deformed, or polar nondeformed ways [Figs. 5(a)–5(c), respectively]. The energies of all three states are expected to be close to each other. Moreover, the director in the polar deformed state presented in Fig. 5(b) is expected to form some waves to fulfill the absence of the global deformation on the large scale. In this sense, the elastic constants of the material capable of formation of all three states are expected to be diminished with respect to those of conventional nematic material.

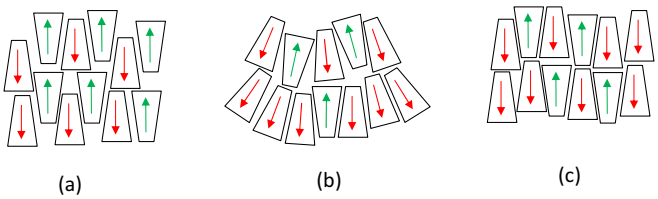

FIG. 5. The local molecular organization of the nonpolar nondeformed (a), polar deformed (b), or polar nondeformed (c) nematic states.

In the case of a splayed structure (b), the splay deformation and the orientational order parameters should vary in the space, since the polar order parameter P [defined in Eq. (6)] is multiplied by $(\nabla\cdot\mathbf{n})$ in Eq. (9). The absolute value of the polar order parameter $|P|$ should intuitively be higher in the areas with the higher absolute value of the splay deformation $|(\nabla\cdot\mathbf{n})|$, while the sign (direction) of both splay deformation and polarization should alternate periodically in space. Since $|P|$ is generally different from one at any coordinate, a part of the molecules [with green arrows in Fig. 5(b)] is always oriented in the opposite direction to the prime molecular orientation [red arrows in Fig. 5(b)], while the nonpolar structure presented in Fig. 5(a) should intuitively correspond (this will be proved in Sec. VI) to the limit case of structure (b) at infinite periodicity. The polar nondeformed structure presented in Fig. 5(c) should intuitively correspond (this also will be proved in Sec. VI) to the situation when the *proper* ferroelectric term in the free energy [the first term in the right-hand side of Eq. (5)], which is independent of the splay, appears to overcome the entropy term.

The director-dependent free-energy density (in this section we do not consider the twist deformation, whose contribution is expected to be very weak in the achiral materials) can be written in the following form, which is a combination of the conventional elastic free energy and the flexoelectric term (9):

$$\begin{aligned} f_{\mathbf{n}} &= \tfrac{1}{2}K_{11}\{\mathbf{n}(\nabla\cdot\mathbf{n}) - \lambda\mathbf{P}\}^2 + \tfrac{1}{2}K_{33}[\mathbf{n}\times[\nabla\times\mathbf{n}]]^2 \\ &= \pm\lambda|P|K_{11}(\nabla\cdot\mathbf{n}) + \tfrac{1}{2}K_{11}(\nabla\cdot\mathbf{n})^2 \\ &\quad + \tfrac{1}{2}K_{33}[\mathbf{n}\times[\nabla\times\mathbf{n}]]^2 + \text{const}, \end{aligned} \tag{10}$$

where $\mathbf{P}$ is the vector having absolute value P [see definition in Eq. (6)] and (at positive P) parallel to a particular direction (one of the two opposite directions) of pseudovector $\mathbf{n}$, K_{11} and K_{33} are the splay and bend elastic constants, respectively, and $K_{11}\lambda \equiv [J^{(1)}_{110} + J^{(1)}_{011}]/3$ is the flexoelectric constant originating from molecular improper polarity [Eq. (9)]. In particular, we expect that polarization can completely originate from the splay deformation. In this case the overall polarization of the sample is equal to zero. For convenience, let us fix the particular direction of pseudovector $\mathbf{n}$. In this case (at positive λ), polarization $\mathbf{P}$ is parallel to director $\mathbf{n}$ at positive splay $(\nabla\cdot\mathbf{n})$ and is antiparallel to $\mathbf{n}$ at negative splay, and thus $+\lambda$ or $-\lambda$ should be chosen appropriately in Eq. (10) for particular half waves.

Following recent publications, Refs. [17,18], and taking also into account the general symmetry arguments, let us consider the cylindrical symmetry of the waves [see tentative

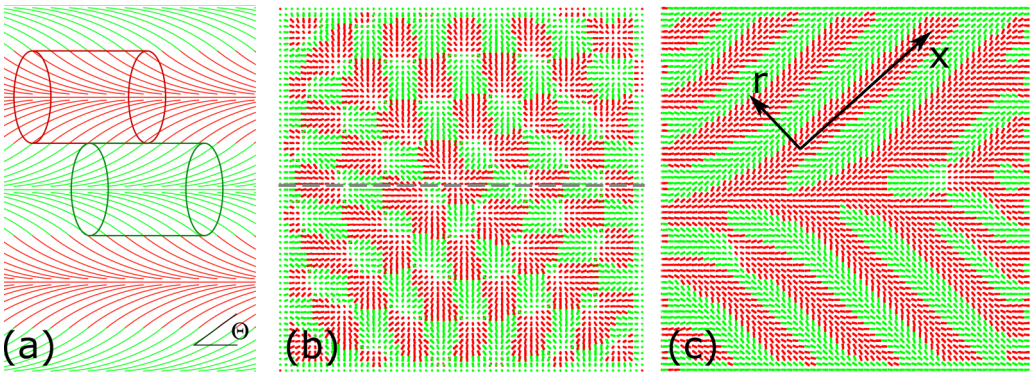

FIG. 6. Tentative illustration of the director distribution in cylindrical waves (a) and snapshots with central cross-cuts of the calculated energy-optimal structure at $|P| = 1$, $\lambda = 20$ (b, c). Red color corresponds to the positive splay and polarization, green color corresponds to the negative splay and polarization. Here θ is the angle between the local director and the cylinder axis x, while r denotes the radial position within the particular cylinder. See details of computer simulations in Sec. V. The planes of images in (b) and (c) are perpendicular to each other.

illustration in Fig. 6(a) and the results of computer simulations at $|P| = 1$ in Figs. 6(b) and 6(c)]. Let us suppose that the material structure represents the cylindrical waves combined without director disruption on the borders between them. Each half wave belongs to a particular cylinder, while the splay and polarization have opposite signs in the neighboring cylinders. Let us say the red cylinder has positive splay and polarization while the green one has negative splay and polarization. From Figs. 6(b) and 6(c) it also follows (it will be proved analytically below) that the highest director deformation is in the center of each cylinder, while the lowest director deformation is on the periphery of each cylinder. Thus the absolute value of polarization arising due to director deformation should also decrease on the periphery of each cylinder, and, in this case, they can stack to each other with minimal energy loss.

Within each cylinder we introduce the r coordinate along its radius, and we expect that the director is (mostly) along the radial planes (the planes parallel to the cylinder axis x and radius r). In this case the director has only two nonzero cylindrical coordinates at each point (the expressions and the subsequent consideration are similar to the Fredericks transition, see particular application in Ref. [19]):

$$n_x = \cos\theta(r), \quad n_r = \sin\theta(r), \tag{11}$$

where the x axis is along the cylinder symmetry axis. From Eq. (11) it follows that

$$\begin{aligned}(\nabla\cdot\mathbf{n}) &= \frac{1}{r}\frac{d(r\,n_r)}{dr} = \frac{1}{r}\sin\theta + \cos\theta\,\frac{d\theta}{dr},\\ (\nabla\cdot\mathbf{n})^2 &= \frac{1}{r^2}\sin^2\theta + \frac{1}{r}\sin(2\theta)\,\frac{d\theta}{dr}\\ &\quad + \cos^2\theta\left(\frac{d\theta}{dr}\right)^2,\\ [\mathbf{n}\times[\nabla\times\mathbf{n}]]^2 &= \left(\frac{dn_x}{dr}\right)^2 = \sin^2\theta\left(\frac{d\theta}{dr}\right)^2.\end{aligned} \tag{12}$$

Substituting Eq. (12) into Eq. (10), neglecting all the terms proportional to either $d\theta/dr$ or to λ (which are expected to have opposite signs in the cylinders with opposite polarization sign, and thus the corresponding terms vanish in average), and minimizing free energy (10) with respect to θ and $d\theta/dr$, as presented, for example, in Ref. [42], Appendix A, one obtains the equation of state in the general form

$$\frac{1}{2}\left(\cos^2\theta + \frac{K_{33}}{K_{11}}\sin^2\theta\right)\left(\frac{d\theta}{dr}\right)^2 - \frac{1}{2}\frac{1}{r^2}\sin^2\theta = k^2, \tag{13}$$

where k is some constant independent of angle θ, which should be obtained by independent minimization of the free-energy density. Introducing a new variable $\psi \equiv k\,r$, one obtains from Eq. (13),

$$\frac{d\theta}{d\psi} = \sqrt{\frac{1+\frac{1}{2\psi^2}\sin^2\theta}{\frac{1}{2}\left(\cos^2\theta + \frac{K_{33}}{K_{11}}\sin^2\theta\right)}}\quad . \tag{14}$$

The equation of state (14) appears to be quite simple. However, in contrast to the case of planar waves, it contains one additional term, which is inversely proportional to the radius, and thus, the splay deformation considerably increases in the middle of each cylinder, but remains finite, because at the axis of each cylinder the director distribution escapes into the axial direction. As a first approximation, let us consider the one-constant approximation ($K_{11} = K_{33} \equiv K$). It will not be difficult to generalize the result for the case of different values of K_{11} and K_{33}. From the very beginning of Eq. (10) for the free-energy density one notes that the whole LC structure can be rescaled by the dimensionless $r\lambda P$ factor without any change in the global free energy. Therefore for the following consideration let us also introduce the dimensionless divergence $(\nabla\cdot\mathbf{n})/(\lambda P)$. The dependencies of angle θ and dimensionless divergence $(\nabla\cdot\mathbf{n})/(\lambda P)$ on the dimensionless radial position $r\lambda P$ within a cylinder, obtained as a result of numerical solution of Eq. (14), are presented in Figs. 7 and 8, respectively. As we predicted, the maximal divergence of director is obtained at the cylinder axis, while the minimal divergence of director is obtained at the cylinder periphery. The dimensionless radius of cylinder, which is the quarter of the wavelength of periodical structure (only a half wave belongs to particular cylinder, while another half wave should belong to the neighboring cylinder) and maximal θ angle

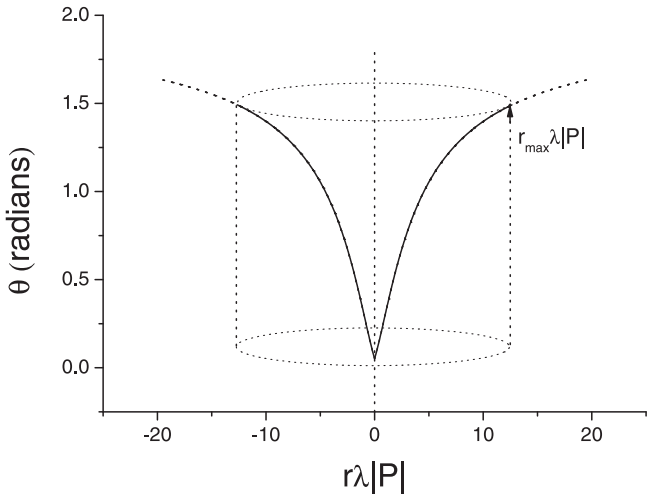

FIG. 7. Dependence of angle θ (see definition in Fig. 6) on the dimensionless radial position within each cylinder at $K_{11} = K_{33}$. The diameter of the cylinder is a half-wave of the periodical structure.

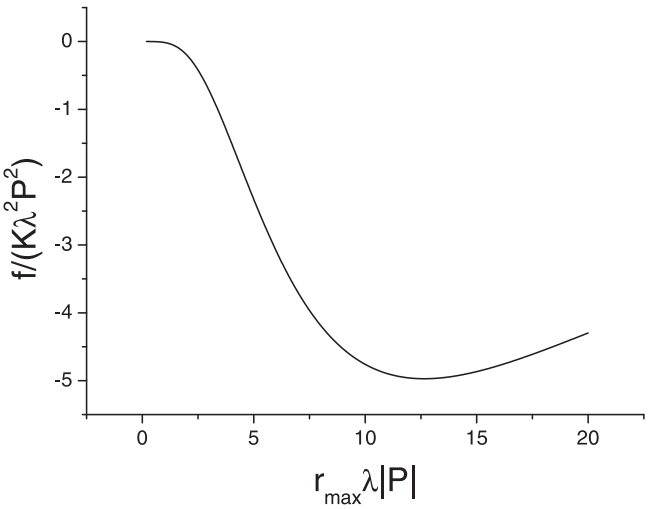

FIG. 9. Average free-energy density having a minimum for the structure with particular $r_{\max}$.

within each wave can be obtained by further minimization of the free-energy density.

Here we suppose that the waves arising in the molecular system are symmetrical with respect to the places where polarization changes its sign. This means that all terms which are proportional either to $d\theta/dr$ or to λ should vanish in average, while all other terms [including the ones proportional to multiple $\lambda\, d\theta/dr$ or to $(d\theta/dr)^2$] should remain. Taking this into account and substituting Eqs. (12) and (14) into Eq. (10), and integrating the free-energy density along the radius of the cylinder (with $r\, dr$ Jacobian), one obtains

$$f_{\mathbf{n}}/(K\lambda^2 P^2) = 2\,\tilde{k}^2 G_1(\psi_m) \pm 2\,\tilde{k}\, G_2(\psi_m), \tag{15}$$

where $\tilde{k} \equiv k\lambda|P|$. We have taken into account that the $r\lambda P$ rescale of structure retains the same overall free energy, and, finally, in the framework of perturbation theory we have split the director and polarization dependencies on the coordinates, while the $G_1(\psi_m)$ and $G_2(\psi_m)$ are introduced as follows:

$$G_1(\psi_m) \equiv \int_0^{\psi_m} \left(1 + \frac{1}{\psi^2}\sin^2\theta\right)\psi\, d\psi,$$
$$G_2(\psi_m) \equiv \int_0^{\psi_m} \psi\cos\theta\frac{d\theta}{d\psi}\, d\psi. \tag{16}$$

Minimizing free-energy density (15) with respect to parameter $\tilde{k}$, one obtains

$$\tilde{k} = \mp\frac{1}{2}\frac{G_2(\psi_m)}{G_1(\psi_m)}, \tag{17}$$

while elimination of parameter $\tilde{k}$ from Eq. (15) yields

$$f_{\mathbf{n}}/(K\lambda^2 P^2) = -\frac{1}{2}\frac{G_2^2(\psi_m)}{G_1(\psi_m)}. \tag{18}$$

The dependence of the dimensionless free-energy density $f_{\mathbf{n}}/(K\lambda^2 P^2)$ on the dimensionless radius $r\lambda|P|$, obtained numerically from Eq. (18) using solution $\theta(\psi)$ of Eq. (14), is presented in Fig. 9. Here the radius $r = \psi/k$ is calculated using Eq. (17). The optimal radius of the cylinder corresponds to the minimum free energy. It is inversely proportional to the flexoelectric constant and polarization, while polarization can depend on the radial position itself. This dependence will be obtained in Sec. VI. On the borders between the neighboring cylinders polarization changes sign, while angle θ starts decreasing, as can also be seen from computer simulation [Figs. 6(b) and 6(c)]. The structure of the neighboring cylinder appears to be the same, but polarization and splay appear to be reversed. One can see from Figs. 7 and 8 that the waves resembling those obtained in computer simulation can arise in cylindrical geometry even in the one-constant approximation. One notes that all dimensionless quantities obtained in this section are expressed in terms of the polar order parameter P, which itself can vary in the space. This variation will be found

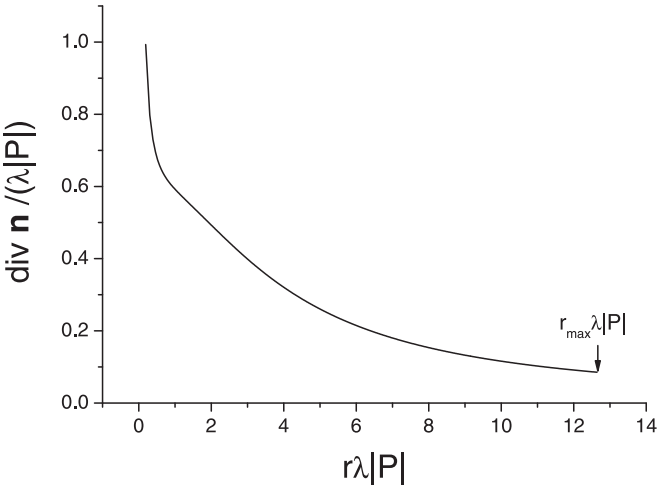

FIG. 8. Dependence of dimensionless divergence $(\nabla\cdot\mathbf{n})/(\lambda|P|)$ on the dimensionless radial position within the cylinder at $K_{11} = K_{33}$. The radius of the cylinder is a quarter of the wave of the periodical structure.

out in Sec. VI within the framework of a molecular-statistical approach.

V. COMPUTER SIMULATIONS

To perform calculations of the bulk structure of polar nematic material, we have modified the existing extended Frank elastic continuum approach [43], previously used for calculations of nematic and cholesteric systems. The original approach includes the effects of the director field distortion and the energy of defects. Here we are also going to take into account the flexoelectric term (see Sec. IV):

$$F = \frac{1}{2}\int_V \{K_{11}(\mathbf{n}(\nabla\cdot\mathbf{n}) - \lambda\,\mathbf{p})^2 + K_{22}(\mathbf{n}\cdot[\nabla\times\mathbf{n}])^2 + K_{33}[\mathbf{n}\times[\nabla\times\mathbf{n}]]^2\}dV + \frac{W}{2}\int_\Omega (1-\cos^2\gamma)d\Omega + F_{\rm def}, \quad (19)$$

where the second powers in the first and third terms in figure brackets mean the dot product of the vector, which is squared, by itself; K_{11}, K_{22}, and K_{33} are the splay, twist, and bend elastic constants, respectively; $K_{11}\lambda$ is the flexoelectric constant; $\mathbf{p}$ is the polarizability direction vector; V is the bulk of the sample having surface Ω; W is the surface anchoring energy density; γ is the angle between the local director and normal to the surface; and $F_{\rm def}$ is the energy of defects calculated by the summation of the point and linear defect energies (see the details in Ref. [43]). For simplicity, the polarizability direction vector $\mathbf{p}$ is supposed to be a unit vector parallel or antiparallel to director $\mathbf{n}$ at each point. Thus, the value of $(\mathbf{n}\cdot\mathbf{p})$, arising when the full square in the first term in figure brackets is open, is equal strictly to 1 or –1. The polarizability direction field is defined on the same cubic lattice as director field $\mathbf{n}$.

Initially, the distributions of $\mathbf{n}$ and $(\mathbf{n}\cdot\mathbf{p})$ are randomized. Then we perform energy optimization using the Metropolis Monte Carlo simulated annealing algorithm. In the original method, Monte Carlo steps trialed random changes in director field $\mathbf{n}$ and were accepted or declined via the Metropolis algorithm. It consequently led to minimization of the total free energy F. In this work each Monte Carlo trial consisted of the same change in director field plus the random change in $(\mathbf{n}\cdot\mathbf{p})$ value. (For both 1 and –1 values, the probability of keeping the same value was 0.5 and the probability of changing to the opposite sign was also 0.5.) As a result, a simulated annealing procedure led to minimization of the free energy over both director $\mathbf{n}$ and polarizability direction $\mathbf{p}$ distributions in a self-consistent way.

A one-constant approximation was used for simplicity: $K_{11} : K_{22} : K_{33} = 1 : 1 : 1$. The value of λ varied from 0 to 20. To take into account potential formation of the disclination lines with the core, its linear energy density was set to $f_{\rm core}^{\rm line} = 10K_{11}$ (see Ref. [43]). The cubic simulation box of size $2\times2\times2$ was rendered into a $64\times64\times64$ lattice. For all facets, boundary conditions were set to a strongly aligned director field along the x axis ($\mu_1 = Wd/K_{11} = 2000$, where d is the cube size). For each value of λ, we produced a 32.7×10^{11} step (10^7 parallel multisteps) Monte Carlo annealing optimization with five independent runs to find the energy-optimal structures.

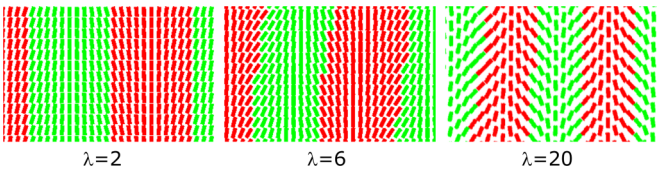

FIG. 10. Structures obtained in computer simulations at $\lambda = 2$, 6, and 20.

The resulting structures are presented in Fig. 10 at several particular values of parameter λ. At $\lambda = 0$ and near zero, the energy-optimal structure is the perfectly oriented nematic with fully random distribution of $(\mathbf{n}\cdot\mathbf{p})$ across the bulk of the simulated system. It makes perfect sense, as the $(\mathbf{n}\cdot\mathbf{p})$ values do not affect the energy at $\lambda = 0$.

In the higher range of parameter λ, the quasiperiodic structures were formed resembling the cylinders with positive and negative $(\mathbf{n}\cdot\mathbf{p})$ placed in a square lattice in a checkerboard pattern. The cross sections of these cylinders are shown in Figs. 6(b) and 6(c) [red and green colors represent the lattice points with negative and positive values of $(\mathbf{n}\cdot\mathbf{p})$, respectively]. The structure of the cylinders is very similar to those obtained in the theoretical part of the paper. In the center of each cylinder, the director is parallel to the principal direction of the cylinder. Near the border between the adjacent cylinders, the director tilts, which effectively generates the splay required for the compensation of a nonzero $\lambda(\mathbf{n}\cdot\mathbf{p})$ term. There are not any point defects or director disclinations in this structure.

The structural changes with the increasing parameter λ demonstrate two important tendencies: (1) the maximum tilt angle increases with the increasing λ, since it is required for the compensation of the corresponding term in the free energy; (2) the cylinder breadth (which is the effective period of the structure) decreases with the increasing λ (see Fig. 11). This dependency is similar to that predicted theoretically in Sec. IV.

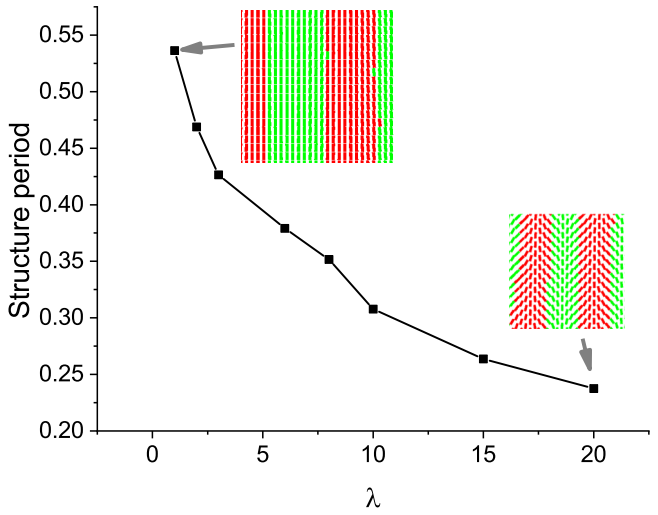

FIG. 11. Period of the structure, obtained in computer simulations, as a function of parameter λ.

VI. ORDER PARAMETERS AND PHASE TRANSITIONS BETWEEN M1, M2, AND MP PHASES

In the present section, the molecular-statistical approach will be considered, and it will be shown how the thermal fluctuations can select between various symmetries discussed in Sec. III and cause the transitions between the MP, M2, and M1 phases. The orientational distribution function [see Eq. (6)] is generally supposed now to have both polar and nonpolar contributions. By minimizing the global free energy with respect to the orientational distribution function in the manner of paper [40], one obtains the following recurrent equations for the nonpolar and polar order parameters:

$$S(\mathbf{r}) = \frac{I_2(\mathbf{r})}{I_0(\mathbf{r})}, \quad P(\mathbf{r}) = \frac{I_1(\mathbf{r})}{I_0(\mathbf{r})}, \tag{20}$$

where

$$I_m(\mathbf{r}) = \int P_m(\mathbf{a}\cdot\mathbf{n}) \exp\left\{-\frac{U_{MF}[(\mathbf{a}\cdot\mathbf{n}),\mathbf{r}]}{k_B T}\right\} d^2\mathbf{a}, \tag{21}$$

where P_m is the mth Legendre polynomial (the first or the second in our particular case). From Eqs. (20) and (21), it follows that the temperature dependencies of the order parameters can be written in the form of Boltzmann distributions in the mean molecular field $U_{MF}[(\mathbf{a}\cdot\mathbf{n}),\mathbf{r}]$ acting on a molecule having orientation of its principal axis $\mathbf{a}$ and located at point $\mathbf{r}$, which consists of the three terms:

$$U_{MF}[(\mathbf{a}\cdot\mathbf{n}),\mathbf{r}] = -\sigma_0\left\{\left[J_{101}^{(0)} + \frac{8\pi V_0}{\sigma_0} K_{11}\lambda^2 \frac{(\nabla\cdot\mathbf{n})}{\lambda P(\mathbf{r})}\right] \times P(\mathbf{r}) P_1(\mathbf{a}\cdot\mathbf{n}) + J_{202}^{(0)} S(\mathbf{r}) P_2(\mathbf{a}\cdot\mathbf{n})\right\}, \tag{22}$$

where σ_0 is the average number of the nearest neighbors of each molecule, and V_0 is the elementary bulk occupied by a molecule and its nearest surrounding. The last term in the figure brackets in Eq. (22) is the nonpolar anisotropy term, which is written exactly in the same form as in the Maier-Saupe theory.

The polar anisotropy term [the first term in the rectangular brackets in Eq. (22)] can be written in the same manner with the only difference that the nonpolar order parameter should be replaced with a polar one and the second Legendre polynomial should be replaced with the first one. The coefficients $J_{101}^{(0)}$ and $J_{202}^{(0)}$ originate from the expansion of the intermolecular potential in spherical invariants [Eqs. (1) and (7)]. The dimensionless divergence of director $(\nabla\cdot\mathbf{n})/(\lambda P)$ is determined as a function of the dimensionless radial position of a molecule within the cylindrical wave in Sec. IV (see Fig. 8). Thus the whole molecular field (22) and the order parameters (20) are determined at any point within the wave if the waves are present. If they are absent, the divergence term in the mean field is equal to zero. The temperature dependencies of the S and P order parameters obtained from Eqs. (20)–(22) are presented in Figs. 12(a) and 12(b), respectively. One notices a good correlation with the experimental results obtained in Refs. [14,15] for the DIO material. The transitions between the M1, M2, and MP phases happen when the temperature decreases. The M1 phase is the conventional nonpolar nematic phase with $S > 0$ and $P = 0$, whose local structure corresponds to the one presented in Fig. 5(a). The MP phase is

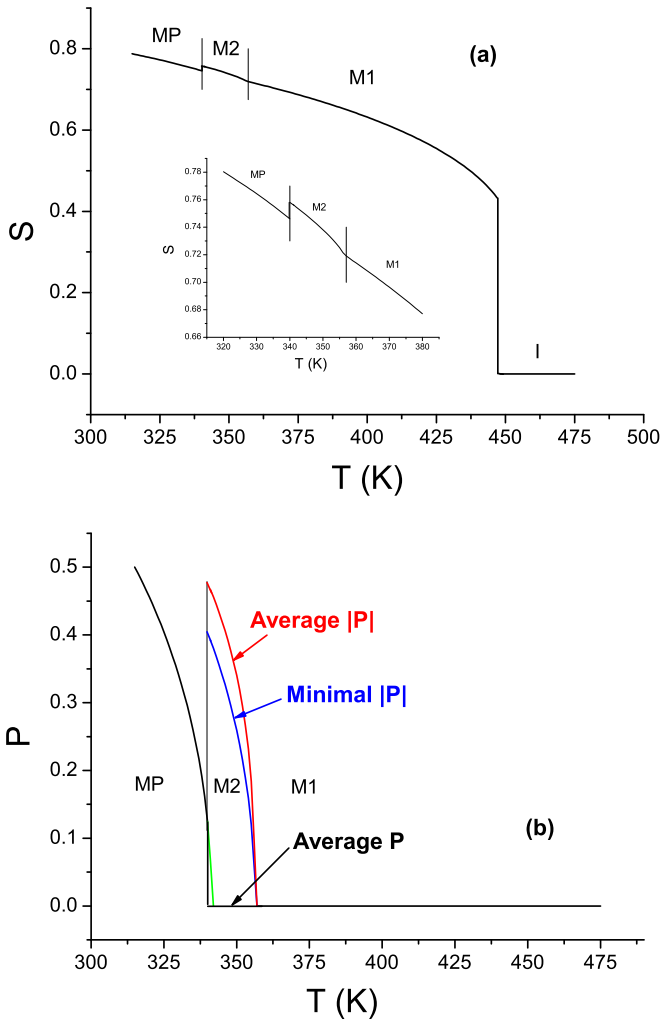

FIG. 12. Temperature dependencies of the nonpolar (a) and polar (b) order parameters at $\sigma_0 J_{202}^{(0)}/k_B = 2032\,\mathrm{K}$, $\sigma_0 J_{101}^{(0)}/k_B = 412\,\mathrm{K}$, $K_{11} = K_{33} = 6\,\mathrm{pN}$, $\lambda = 5\,\mu\mathrm{m}^{-1}$, $J_A/k_B = 130\,\mathrm{K}\,\mu\mathrm{m}$, and $V_0 = 1.1 \times 10^{-24}\,\mathrm{m}^3$ [40].

a proper ferroelectric nematic phase with $S > 0$ and $P \neq 0$ without splay and bend director deformations, whose local structure corresponds to that presented in Fig. 5(c). The M2 phase appears to be the splay phase with antiferroelectric domains (at a particular half wave the polarization is positive, and at the neighboring half wave the polarization is negative). The local structure of the M2 phase corresponds to that presented in Fig. 5(b), while on the larger scale the structure represents the cylindrical waves (domains) demonstrated in Fig. 6. The number of domains with positive splay and polarization is equal to the number of domains with negative splay and polarization. The average P is equal to 0 in the M2 phase [black curve in Fig. 12(b)], while the average $|P|$ [red curve in Fig. 12(b)] is different from zero because of the existence of antiferroelectric domains. It appears to be even larger than in MP, because both $J_{101}^{(0)}$ and $K_{11}\lambda$ contributions are different from zero in M2. Because of the same reason, the nonpolar order parameter S is larger in M2 than in MP. However, the residual orientational ordering reflecting both S and P can appear larger in MP than in M2. Both S and P

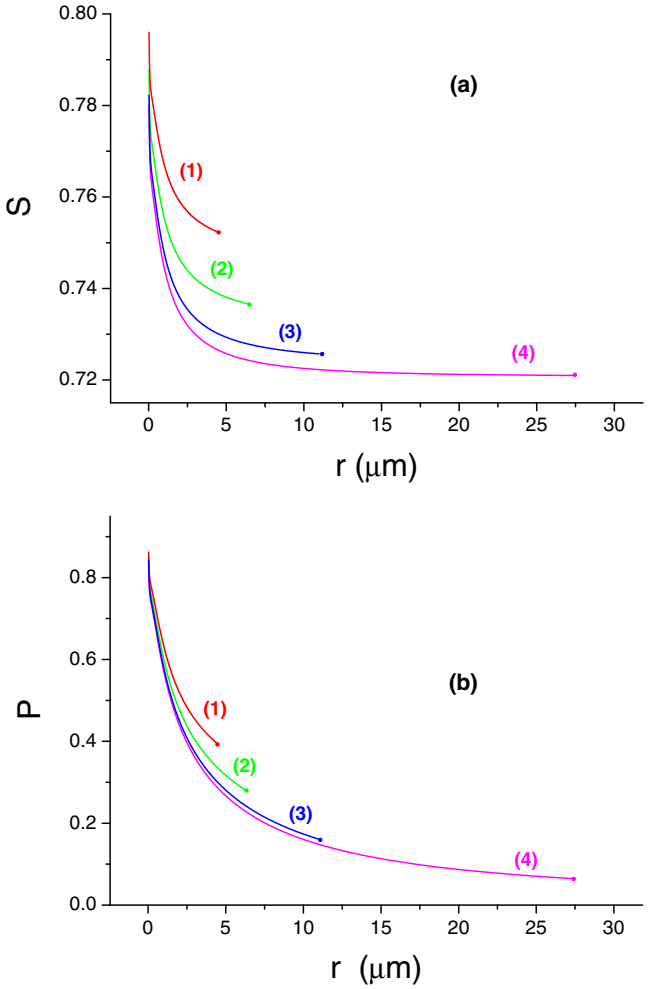

FIG. 13. Dependencies of the nonpolar (a) and polar (b) order parameters on the radial position within each cylindrical wave in the M2 phase at $\sigma_0 J^{(0)}_{202}/k_B = 2032\,\mathrm{K}$, $\sigma_0 J^{(0)}_{101}/k_B = 412\,\mathrm{K}$, $K_{11} = K_{33} = 6\,\mathrm{pN}$, $\lambda = 5\,\mu\mathrm{m}^{-1}$, $J_A/k_B = 130\,\mathrm{K}\,\mu\mathrm{m}$, $V_0 = 1.1 \times 10^{-24}\,\mathrm{m}^3$ [40], and $T = 341\,\mathrm{K}$ [curves (1)], 349 K [curves (2)], 354 K [curves (3)], and 356 K [curves (4)]. Dots at the end of each curve correspond to the domain radius at each particular temperature.

order parameters contribute to the optical anisotropy. Since parameter P greatly increases at the M2-MP phase transition, the optical anisotropy also increases that corresponds to the observations presented in Fig. 2.

To outline the origin of the transitions between the M1, M2, and MP phases, one should pay attention to Fig. 13, in which the S and P order parameters are presented at several particular temperatures as functions of the radial position within the cylindrical waves (domains) arising in the M2 phase. Both nonpolar and absolute value of polar order parameters are larger in the center of each cylinder and smaller on the periphery of each cylinder. The smallest absolute value of polar order parameter (which is on the periphery of cylinder) is also presented as a function of temperature by the blue curve in Fig. 12(b). Between cylinders the polarization is supposed to change sign so that unfavorable antiferroelectric decoupling should exist at each stacking area between cylinders. The equilibrium free-energy density at radial position r inside of each cylinder can also be obtained by analogy to that presented in Ref. [40]:

$$4\pi V_0 f(r) = -k_B T \ln I_0(r) + \frac{1}{2}\sigma_0 \left\{ \left[J^{(0)}_{101} + \frac{8\pi V_0}{\sigma_0} K_{11}\lambda^2 \frac{(\nabla \cdot \mathbf{n})}{\lambda P(r)} \right] P^2(r) + J^{(0)}_{202} S^2(r) \right\}, \tag{23}$$

while the junctions between neighboring cylinders should correspond to unfavorable antiferroelectric orderings whose surface energy density is proportional to $P^2(r_{\max})$ with positive sign, so that the average free-energy density should be recalculated as

$$4\pi V_0 \langle f(r) \rangle = \frac{8\pi V_0}{r^2_{\max}} \int_0^{r_{\max}} f(r) r\, dr + J_A \frac{P^2(r_{\max})}{r_{\max}}, \tag{24}$$

where J_A is the strength of antiferroelectric decoupling. The transition temperatures between M1, M2, and MP are determined from the comparison of the free energies (23)–(24) in all phases. The first term in the right-hand side of Eq. (24) is the average over each cylinder free-energy density, while the second term is the antiferroelectric decoupling term, which is inversely proportional to the radius of each cylinder $r_{\max}$ decreasing with the decreasing temperature, since it is inversely proportional to the absolute value of polarization. The size of each domain decreases with the decreasing temperature, which is why the borders between domains make larger and larger contribution to the average free-energy density. At some sufficiently low temperature, this positive contribution becomes larger than the difference between the bulk free energies [corresponding to the first term in Eq. (24)] of the MP and M2, and the first-order phase transition from M2 to MP happens. Without the splay deformation, the polar order parameter would vary with variation of temperature as shown by green line in Fig. 12(b). Since the range of the green curve is very narrow in the temperature scale, the polarization in most of the temperature range of the M2 phase exists solely due to the splay deformation.

The radius of each cylinder as a function of temperature within the M2 phase is presented in Fig. 14, from where one concludes that the wavelength of director deformation diverges at the transition temperature between the M2 and M1 phases, the polar order parameter at each coordinate tends to zero, and the second-order transition from the M2 phase to M1 phase happens. A particular elastic constant specific to a conventional nematic phase in the one-constant approximation was used in calculation of Figs. 12–14. As a result, the radius of the cylindrical domain within the M2 phase mostly varies from several micrometers to several tens of micrometers depending on the temperature. The domain size appears to be of the same order of magnitude as measured experimentally in Ref. [15]. However, in the polar materials, because of the existence of the three different structures presented in Fig. 5 with almost equal free energy, which can transform to each other by means of the splay and bend deformations, we expect that both the splay and bend elastic constant can be sufficiently smaller than those in conventional materials. Moreover, since the transition between (a) and (b) structures is of the second order, there is no energy barrier between them. This effect was

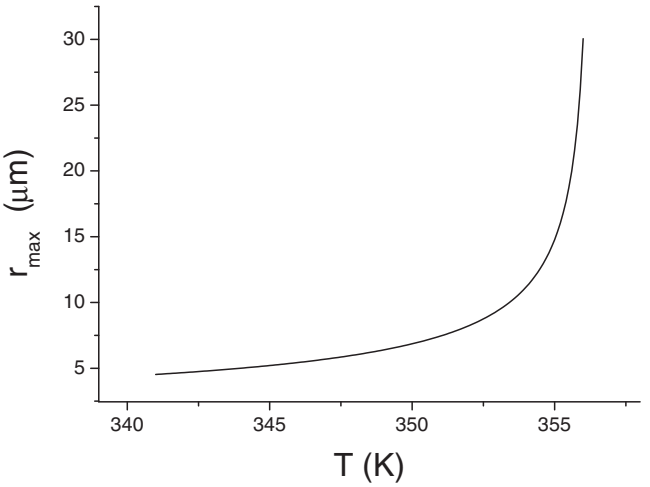

FIG. 14. Temperature dependence of the domain radius within the M2 phase at $\sigma_0 J^{(0)}_{202}/k_B = 2032\,\mathrm{K}$, $\sigma_0 J^{(0)}_{101}/k_B = 412\,\mathrm{K}$, $K_{11} = K_{33} = 6\,\mathrm{pN}$, $\lambda = 5\,\mu\mathrm{m}^{-1}$, $J_A/k_B = 130\,\mathrm{K}\,\mu\mathrm{m}$, and $V_0 = 1.1 \times 10^{-24}\,\mathrm{m}^3$ [40].

previously formulated by Čopič and Mertelj [37] as elastic constant softening. In this case, the domain size will reduce as a square root of the elastic constant decrease. The $J^{(0)}_{202}$, $J^{(0)}_{101}$, $K_{11}\lambda^2$, and J_A parameters were chosen to match the three transition temperatures measured in Refs. [14,15] and in our own experiment, and also the expected temperature at which the MP and M1 phases would coexist in the absence of the M2 phase [the place where the green curve in Fig. 12(b) comes to zero].

VII. CONCLUSION

In the present paper, a comprehensive investigation of the paraelectric, improper antiferroelectric ("splay"), and proper ferroelectric nematic phases in the materials composed of polar molecules was done, including experiment, theory, and computer simulations. Here we refer to these phases as M1, M2, and MP, respectively, similar to that suggested in Ref. [14]. The origin and structures of the M1, M2, and MP phases were outlined. The higher-temperature M1 phase is the conventional nonpolar nematic phase with equal proportions of polar molecules with principal polar axes belonging to both semispheres perpendicular to director. The lower-temperature MP phase is the proper ferroelectric phase without splay and bend director deformations. An intermediate, M2 phase is the improper antiferroelectric nematic phase with very high local polar and nonpolar order parameters. The polarization in the M2 phases arises mostly due to the splay director deformation. The director exhibits the splay and bend deformations in the form of cylindrical waves, which are, in fact, the same as the double splay reported by Rosseto and Selinger [35,36]. On average, the polarization is equal to zero in the M2 phase, while it is nonzero within each cylinder forming a half wave. The absolute values of polarization and splay deformation are maximal in the middle of each cylinder and are minimal on the periphery of each cylinder. Between the cylinders, the polarization changes its direction. The numbers of the cylinders with positive and negative polarization are equal. The director distribution within each cylinder was obtained analytically and from computer simulations. An excellent correlation between computer simulations and theory was found.

The intermolecular interactions of specific symmetry responsible for the proper and improper ferroelectricity were found. The nonpolar and polar order parameters were estimated in the M1, M2, and MP phases as functions of temperature within the framework of a molecular-statistical approach. The transitions between the M1, M2, and MP phases upon the decrease of the temperature were identified, and their origins were outlined. In the M2 phase, both nonpolar and polar order parameters vary in the space, and their variation was estimated. The equilibrium domain size (cylinder diameter) in the M2 phase was found to increase with the increasing temperature and to diverge at the M2-M1 transition temperature. Polarization vanishes at each point in the space at the same temperature. Although the phenomenological output of our theory is similar to that presented in Refs. [34–36], consideration of statistical distributions results in the second-order M1-M2 phase transition. Here we understand that the divergence of domain size is always a sort of theoretical idealization, and therefore our results are quite consistent with the conclusion made in Ref. [33] about the weak first-order phase transition between these phases.

The M2-MP phase transition is of the first order. It happens because of the antiferroelectric decoupling at the junction areas between the domains. The junction areas become denser at the decreasing domain size (with the decreasing temperature within M2), and their positive contribution to the free energy becomes more and more valuable. Finally, they destroy the M2 phase at a particular temperature and the proper ferroelectric MP phase arises instead. The transition temperatures between the M1, M2, and MP phases were identified experimentally for the DIO material (see also Ref. [14]), and the order of the phase transition was checked. A very good correlation between theory and experiment is found. However, experimental determination of the elastic constants in polar materials appears to be of the prime importance in future publications, since the domain size in the M2 phase is proportional to the square root of the splay elastic constant.

ACKNOWLEDGMENTS

A.V.E. and S.A.Sh. thank the Russian Science Foundation (Project No. 22-23-00391) for the financial support of theoretical investigations presented in this work. V.Yu.R. thanks the Russian Foundation for Basic Research (Project No. 21-53-50008) for the financial support of computer simulations presented in this work. F.A., H.N., and K.I. thank the Japan Society for the Promotion of Science (Project No. JPJSBP120214814) for the financial support of experimental investigation presented in this work. F.A. and H.N. thank JSPS KAKENHI (JP19K15438; H.N. and JP21H01801; F.A.), Incentive Research Projects in RIKEN (100689; H.N.) and JST CREST (JPMJCR17N1; F.A.) for the financial support of synthesis of the material used in this work. This research was carried out using the equipment of the shared research facilities of HPC computing resources at Lomonosov Moscow State University.

[1] H.-W. Chen, J.-H. Lee, B.-Y. Lin, S. Chen, and S.-T. Wu, Light Sci. Appl. **7**, 17168 (2018).

[2] Y. Garbovskiy, J. R. Baptist, J. Thompson, T. Hunter, J. H. Lim, Seong Gi Min, J. B. Wiley, L. M. Malkinski, A. Glushchenko, and Z. Celinski, Appl. Phys. Lett. **101**, 181109 (2012).

[3] Y. S. Zhang, C. Y. Liu, A. V. Emelyanenko, and J.-H. Liu, Adv. Funct. Mater. **28**, 1706994 (2018).

[4] Y. Garbovskiy and A. Glushchenko, Proc. SPIE **10941**, 1094109 (2019).

[5] B. Wang, G. Zhang, A. Glushchenko, J. L. West, P. J. Bos, and P. F. McManamon, Appl. Opt. **44**, 7754 (2005).

[6] O. Melnyk, R. Jones, R. Macedo, Y. Garbovskiy, G. Hagen, A. V. Glushchenko, K. Spendier, and R. E. Camley, ACS Photonics **8**, 1222 (2021).

[7] A. Glushchenko, O. P. Boiko, B. Ya. Lenyk, A. Senenko, and V. G. Nazarenko, Appl. Phys. Lett. **117**, 071902 (2020).

[8] C. Esteves, E. Ramou, A. R. P. Porteira, A. J. Moura Barbosa, and A. C. A. Roque, Adv. Opt. Mater. **8**, 1902117 (2020).

[9] S. A. Shvetsov, V. Yu. Rudyak, A. V. Emelyanenko, N. I. Boiko, Y.-S. Zhang, J.-H. Liu, and A. R. Khokhlov, J. Mol. Liq. **267**, 222 (2018).

[10] S. A. Shvetsov, A. V. Emelyanenko, N. I. Boiko, J.-H. Liu, and A. R. Khokhlov, J. Chem. Phys. **146**, 211104 (2017).

[11] V. Yu. Rudyak, M. N. Krakhalev, V. S. Sutormin, O. O. Prishchepa, V. Ya. Zyryanov, J.-H. Liu, A. V. Emelyanenko, and A. R. Khokhlov, Phys. Rev. E **96**, 052701 (2017).

[12] R. Camley, Z. Celinski, Y. Garbovskiy, and A. Glushchenko, Liq. Cryst. Rev. **6**, 17 (2018).

[13] O. Melnyk, Yu. Garbovskiy, D. Bueno-Baques, and A. Glushchenko, Crystals **9**, 314 (2019).

[14] H. Nishikawa, K. Shiroshita, H. Higuchi, Y. Okumura, Y. Haseba, S.-ichi Yamamoto, K. Sago, and H. Kikuchi, Adv. Mater. **29**, 1702354 (2017).

[15] S. Brown, E. Cruickshank, J. M. D. Storey, C. T. Imrie, D. Pociecha, M. Majewska, A. Makal, and E. Gorecka, ChemPhysChem **22**, 1 (2021).

[16] H. Nishikawa and F. Araoka, Adv. Mater. **33**, 2101305 (2021).

[17] J. Li, H. Nishikawa, J. Kougo, J. Zhou, S. Dai, W. Tang, X. Zhao, Y. Hisai, M. Huang, and S. Aya, Sci. Adv. **7**, 17 (2021).

[18] X. Zhao, J. Zhou, J. Li, J. Kougo, Z. Wan, M. Huang, and S. Aya, Proc. Natl. Acad. Sci. **118**, e2111101118 (2021).

[19] Y. Garbovskiy, A. V. Emelyanenko, and A. Glushchenko, Nanoscale **12**, 16438 (2020).

[20] R. B. Meyer, Phys. Rev. Lett. **22**, 918 (1969).

[21] R. B. Meyer, Mol. Cryst. Liq. Cryst. **40**, 33 (1977).

[22] A. D. L. Chandani, Y. Ouchi, H. Takezoe, A. Fukuda, K. Terashima, K. Furukawa, and A. Kishi, Jpn. J. Appl. Phys., Part 2 **28**, L1261 (1989).

[23] A. D. L. Chandani, E. Gorecka, Y. Ouchi, H. Takezoe, and A. Fukuda, Jpn. J. Appl. Phys., Part 2 **28**, L1265 (1989).

[24] E. Gorecka, A. Chandani, Y. Ouchi, H. Takezoe, and A. Fukuda, Jpn. J. Appl. Phys., Part 1 **29**, 131 (1990).

[25] A. V. Emelyanenko, Ferroelectrics **495**, 129 (2016).

[26] V. Novotna, M. Glogarova, V. Hamplova, and M. Kaspar, J. Chem. Phys. **115**, 9036 (2001).

[27] D. Catalano, V. Domenici, A. Marini, C. A. Veracini, A. Bubnov, and M. Glogarova, J. Phys. Chem. B **110**, 16459 (2006).

[28] A. Bubnov, V. Novotna, V. Hamplova, M. Kaspar, and M. Glogarova, J. Mol. Struct. **892**, 151 (2008).

[29] Y. Na, Y. Naruse, N. Fukuda, H. Orihara, A. Fajar, V. Hamplova, M. Kaspar, and M. Glogarova, Ferroelectrics **364**, 13 (2008).

[30] A. V. Emelyanenko, Crystals **9**, 583 (2019).

[31] S. Dhakal and J. V. Selinger, Phys. Rev. E **81**, 031704 (2010).

[32] A. Mertelj, L. Cmok, N. Sebastian, R. J. Mandle, R. R. Parker, A. C. Whitwood, J. W. Goodby, and M. Copic, Phys. Rev. X **8**, 041025 (2018).

[33] R. J. Mandle and A. Mertelj, Phys. Chem. Chem. Phys. **21**, 18769 (2019).

[34] N. Sebastian, L. Cmok, R. J. Mandle, M. R. de la Fuente, I. Drevense Olenik, M. Copic, and A. Mertelj, Phys. Rev. Lett. **124**, 037801 (2020).

[35] M. P. Rosseto and J. V. Selinger, Phys. Rev. E **101**, 052707 (2020).

[36] J. V. Selinger, Annu. Rev. Condens. Matter Phys. **13**, 49 (2022).

[37] M. Čopič and A. Mertelj, Phys. Rev. E **101**, 022704 (2020).

[38] A. V. Emelyanenko and A. R. Khokhlov, J. Chem. Phys. **142**, 204905 (2015).

[39] N. V. Kalinin, A. V. Emelyanenko, and J.-H. Liu, Phase Trans. **90**, 86 (2017).

[40] A. V. Emelyanenko, E. S. Filimonova, and A. R. Khokhlov, Phys. Rev. E **103**, 022709 (2021).

[41] M. S. Romashin and A. V. Emelyanenko, Moscow Univ. Phys. **68**, 249 (2013).

[42] A. V. Emelyanenko, Phys. Rev. E **82**, 031710 (2010).

[43] V. Yu. Rudyak, A. V. Emelyanenko, and V. A. Loiko, Phys. Rev. E **88**, 052501 (2013).